Global gridded NO$_x$ emissions using TROPOMI observations

Anthony Rey-Pommier[1], Alexandre Héraud[1], Frédéric Chevallier[1], Philippe Ciais[1,2], Theodoros Christoudias[2], Jonilda Kushta[2] and Jean Sciare[2].

[1] Laboratoire des Sciences du Climat et de l'Environnement, LSCE/IPSL, CEA-CNRS-UVSQ, Université Paris-Saclay, 91190 Gif-sur-Yvette, France
[2] The Cyprus Institute, Climate and Atmosphere Research Center, 2121 Nicosia, Cyprus

Correspondence: Anthony Rey-Pommier (`anthony.rey-pommier@lsce.ipsl.fr`)

Abstract. We present top-down global gridded emissions of NO$_x$ for the year 2022. This dataset is constructed from retrievals of tropospheric vertical column densities of NO$_2$ by the TROPOMI spaceborne instrument associated with winds and atmospheric composition data from ECMWF reanalyses, using an improved version of a mass-balance atmospheric inversion. The emissions are provided with a spatial resolution of 0.0625°×0.0625° and deliver a detailed overview of the distribution of emissions. They allow the identification of intense area sources and isolated emitters, and the quantification of their associated emissions. At global level, the emissions obtained are consistent with the EDGARv6.1 bottom-up inventory, although there are differences at regional level, particularly in emerging countries and countries with low observation densities. The three largest emitting countries, China, the United States and India, are 11, 16 and 6% lower than EDGAR estimates. Uncertainties remain high, and a quantitative analysis of emissions over several averaging periods indicates that averaging emissions uniformly across the year may be sufficient to obtain estimates consistent with annual averages, in regions of the world with high retrieval densities. This dataset is designed to be updated with a low latency to help policymakers monitor emissions and implement energy savings and clean air quality policies. The data can be accessed at `https://doi.org/10.5281/zenodo.13957837` as monthly files (Rey-Pommier et al., 2024).

1 Introduction

Air pollution is one of the leading causes of premature death in the world. Public health policies, implemented at the scale of countries, regions or cities, often aim to reduce the exposure to several pollutants, such as nitrogen oxides (NO$_x$ = NO+NO$_2$). Such mitigation plans therefore require a precise knowledge of the emitters, as well as a monitoring of their emission levels over time. Data on NO$_x$ emissions is therefore fundamental for monitoring the implementation of air quality policies. Besides, because NO$_x$ is mainly produced during the combustion of carbon fuels at high temperatures, such data can also be a tool to measure progress towards carbon neutrality. Gridded emissions with high spatial and temporal resolution are therefore of great scientific and political value. Many of such datasets are emission inventories, i.e. bottom-up models in which emissions are calculated on the basis of known sectoral activities and allocated in time and space, combined with specific emission factors by sector and, possibly, by country. These inventories provide valuable information on long-term trends and large-scale emission budgets, but they suffer from several weaknesses. They hardly represent daily or weekly variations, their activity data may be outdated, and some sources may be misallocated or unknown, which is common in many developing countries. Besides, uncertainties surrounding rapidly changing emissions factors and the generally low temporal resolution of activity data limits, in certain circumstances, the realism of such bottom-up inventories. Finally, they have a data lag of at least one year, which limits their potential as monitoring tools.

In this context, increasing efforts have been made to overcome the weaknesses of the inventories in order to obtain independent emission datasets that are homogeneous from one country to another. Such datasets are of the top-down type: they use direct observations of pollution and result from the inversion of an atmospheric chemistry-transport model (CTM) in which these atmospheric observations are assimilated. The observation data may be in-situ measurements or satellite retrievals.

In previous studies, we used a method for detecting and quantifying NO_x emissions from daily observations of NO_2 columns by the TROPOMI instrument, onboard the Sentinel 5P instrument. This method, developed for the countries of the Eastern Mediterranean and Middle East region, is based on a two-dimensional simplification of atmospheric chemistry and transport, and does not require the direct use of a full 3D chemistry-transport model. Here, we extend the emissions domain to the whole world for the year 2022, and provide a dataset of averaged NO_x emissions at a resolution of 0.0625°×0.0625°. We analyse the results by pinpointing emitters and distinguishing between point sources, generally corresponding to isolated industrial facilities, and diffuse/area sources, generally corresponding to megacities. We also compare the results with the bottom-up inventory EDGARv6.1 and assess their reliability using different average horizons.

This article is structured as follows: Section 2 details the method used throughout this study, its improvements and simplifications since its previous uses, and the input data in its implementation. Section 3 presents the global NO_x emissions dataset and analyses the different types of emitters. It also compares the results obtained with the EDGARv6.1 bottom-up inventory, and analyses different time horizons for averaging daily emissions in order to obtain representative results. Section 4 analyses the applicability limits of the method and highlights sources of uncertainty.

2 Methods

2.1 Input data

2.1.1 TROPOMI NO_2 column densities

NO_2 can be observed from space with satellite instruments based on its strong absorption features in the 400–465 nm wavelength region (Vandaele et al., 1998). By comparing observed spectra with a reference spectrum, the amount of NO_2 in a portion of the atmosphere between the instrument and the surface can be derived. The TROPOspheric Monitoring Instrument (TROPOMI), onboard the European Space Agency's (ESA) Sentinel-5 Precursor (S-5P) satellite, is one of those instruments. This instrument has a large swath width (∼2600 km), combined with the 15-day orbit cycle of the satellite, leading to a revisit time of one day for every point of the Earth in absence of clouds. Moreover, these daily measurements are always collected during the middle of the day, the satellite crossing the sunlit equator at around 13:30 local time (LT). The high spatial resolution of the instrument (3.5×5.5 km² since 6 August 2019) allows observing fine-scale structures of NO_2 pollution, such as hotspots within medium-size cities or plumes from power plants and industrial facilities. Tropospheric vertical column densities (VCDs, or simply "columns") are provided after retrieval of total slant column densities using the Differential Optical Absorption Spectroscopy method (Platt et al., 2008). VCDs represent the integrated number of NO_2 molecules per surface unit between the surface and the tropopause at the corresponding vertical. An algorithm also supplies an air mass factor, which is the ratio between slant and vertical column densities. This factor is derived from the knowledge of many physical quantities such as the vertical distribution of the absorber but also the viewing angle and the albedo of the observed surface. It comprises a significant part of the uncertainty in NO_2 measurements (Boersma et al., 2004; Lorente et al., 2019), which becomes non-negligible in a polluted atmosphere. Each TROPOMI retrieval is also associated with a quality assurance value q_a, which ranges from 0 (no data) to 1 (high-quality data). We selected NO_2 retrievals with q_a values greater than $q_{a,\mathrm{lim}} = 0.75$, which correspond to clear-sky conditions (Eskes et al., 2022). Here, we use TROPOMI NO_2 retrievals in 2022 (OFFL product using processor version 2.5.0, product version 2.3.1 and 2.4.0 before and after November 2022 respectively). To limit effects due to product of processor version changes, other years are not studied.

2.1.2 Meteorological and air composition fields

Horizontal wind is taken from the ERA5 data archive, provided by the European Centre for Medium-Range Weather Forecasts (ECMWF). Both components have a horizontal resolution of 0.25°×0.25° gridded on 37 vertical pressure levels (Hersbach et al., 2020). ECMWF also produces a reanalysis for air composition, under the Copernicus Atmospheric Monitoring Service (CAMS). It provides analyses and forecasts for reactive gases, greenhouse gases and aerosols. These parameters are gridded on 25 vertical pressure levels with a horizontal resolution of 0.4°×0.4° and a temporal resolution of 3 hours (Huijnen et al., 2016). Here, ground concentrations of NO_2, NO, OH, as well as temperature, are taken from CAMS to represent chemical processes in our model.

2.1.3 Elevation data

For computing altitude gradients, we use the Global Multi-resolution Terrain Elevation Data (GMTED2010, Danielson and Gesch (2011)). Elevation data is regridded on the TROPOMI grid, before calculation of the corresponding gradient

93 to derive a corrective "topography-wind" value that is detailed in Section 2.2.2.

2.2 The mass-balance inversion

2.2.1 Main principle

96 The flux-divergence method is a mass-balance inversion model calculating the emissions of a given trace gas from
97 observations of the corresponding vertical tropospheric columns, which is particularly well suited to data with high
98 spatial resolution. In the case of NO_2, this approach was pioneered by Beirle et al. (2019). It has subsequently been
99 implemented differently by other researchers, in different circumstances under simplified forms or, on the contrary,
100 more complex ones (Lama et al., 2020; Rey-Pommier et al., 2022; de Foy and Schauer, 2022; Sun, 2022). The flux-
101 divergence method is based on the conservation of mass principle, which makes it possible to calculate emission
102 densities at the pixel scale as a function of a transport term and a sink term. By noting C the local concentration of
103 NO_2 and $\mathbf{w} = (u, v, w)$ the mean wind at the time of measurement, the corresponding emissions E_C are expressed as:

$$E_C = \frac{\partial C}{\partial t} + \mathrm{div}(C\mathbf{w}) + S_C \tag{1}$$

104 Here S_C is the sink term expressing the loss of NO_2 due to chemical reactions. Assuming that the vertical variations
105 in concentration are small compared with the horizontal variations, and considering that most NO_2 remains confined
106 close to the ground, the previous equation can be rewritten in terms of tropospheric columns Ω, which enables, in
107 steady state, the computation of emissions per surface area E, as:

$$E = \frac{\partial(\Omega u)}{\partial x} + \frac{\partial(\Omega v)}{\partial y} + S_\Omega \tag{2}$$

108 S_Ω is the sink term expressed by surface unit. $D = \frac{\partial(\Omega u)}{\partial x} + \frac{\partial(\Omega v)}{\partial y}$ is the horizontal advection (transport) term. The
109 assumption of a stationary state and a pollution concentration close to the ground means that the temporal and vertical
110 dimensions of the problem can be ignored, resulting in a purely horizontal calculation of emissions. The corresponding
111 reduction in complexity means that inversions can be performed very quickly compared with the conventional use
112 of full-fledged 3D CTMs and without *a priori* knowledge on emissions. On the downside, such simplifications are
113 accompanied by uncertainties, the main sources of which being uncertainties on the input tropospheric columns, wind
114 direction and atmospheric composition.

115   Finally, we convert the NO_2 production into NO_x emissions. Performing this conversion is accounting for the
116 portion of NO_x, mainly emitted as NO, which is not converted into NO_2 by reaction with ozone. The reformation
117 of NO by the photolysis of NO_2 during the day leads to an equilibrium between the two compounds. The ratio
118 $\mathcal{L} = [NO_x]/[NO_2]$ which usually varies between 1.2 and 1.4, depending on local conditions. NO_x emissions are
119 therefore calculated as:

$$E_{NO_x} = \mathcal{L}E \tag{3}$$

120 In most urbanized areas, daytime NO concentrations frequently exceed 20 ppb. Under such conditions, this ratio is
121 stabilized in a few minutes (Graedel et al., 1976; Seinfeld and Pandis, 2006). As this time is shorter than the inter-mesh
122 transport timescale, the impact of stabilization time on the overall emission composition can be justifiably ignored.
123 However, this assumption breaks down near emission sources, where the stationary hypothesis may not be applicable,
124 and the value of $\mathcal{L}$ could be significantly higher than 1.4. The implications of this neglect will be discussed in Section
125 4.1.

2.2.2 Refined version

127 In order to consider only anthropogenic pollution located close to the ground, it is necessary to remove any signal of
128 natural emissions from the tropospheric columns provided by TROPOMI. In the absence of anthropogenic sources,
129 the NO_2 columns that are observed constitute a tropospheric background Ω_b. At the global scale, this background is
130 mostly due to soil emissions in the lower troposphere (Yienger and Levy, 1995; Hoelzemann et al., 2004). In the upper
131 troposphere, NO_2 sources include lightning, convective injection and downwelling from the stratosphere (Ehhalt et al.,
132 1992). We remove that background by calculating the 1st tercile in a 200 pixel × 430 pixel zone around each pixel
133 (along × across track, i.e. approx. 700 km × 2360 km). We assume that this zone is sufficiently large whatever the
134 considered pixel so that this tercile corresponds to the typical local value for this background. We then subtract this
135 background to the calculated tropospheric column densities and use the resulting lower tropospheric vertical density

136 $\Omega' = \Omega - \Omega_b$ in the flux divergence method. Such assumption can be challenged above macro-regions for which soil
137 emissions and wildfires result in high NO_2 values observed by TROPOMI (those emissions are therefore considered
138 abusively as anthropogenic sources). This can also happen around shipping lanes where exhaust particles increase the
139 likelihood of thunderstorms (Thornton et al., 2017). The neglect of such effects is highlighted in Section 4.1.

140 We represent the sink term S_Ω by considering only the chemical loss of NO_2 due to its reaction with the hydroxyl
141 radical (OH). This reaction follows a first-order kinetics, and the sink term can be expressed as $S_\Omega = k_{OH+NO_2}[OH]$
142 with k_{OH+NO_2} the reaction rate whose value is given by Burkholder et al. (2020). This is equivalent to compute a
143 mixed lifetime $\tau = 1/(k_{OH+NO_2}[OH])$, which generally ranges between 1 and 12h. In many studies, this quantity is
144 kept uniform and constant in the use of the flux-divergence method (Beirle et al., 2019; de Foy and Schauer, 2022).
145 Here, a singularity of our version of the flux-divergence method is to account for the temporal variability of OH, which
146 is primarily driven by the amount of UV radiation from the stratosphere, but also for its spatial variability, since OH
147 can also be influenced by NO_x through a non-linear relationship (Valin et al., 2011). In this respect, our sink term
148 is heavily reliant on the NO_x sources accounted for in CAMS data. Neglecting a source, or mis-estimating the order
149 of magnitude of its NO_x emissions, therefore results in a wrong OH field whose bias depends on the amplitude of the
150 neglect. Similarly, the coarse resolution in CAMS data ($0.4° \times 0.4°$) can fail to represent pollution gradients downwind
151 different sources, leading to a wrong estimation of the real OH budget. We expect these effects to be minor compared
152 to those that would result in representing a constant lifetime for NO_2 which oversimplifies and misrepresents temporal
153 and spatial dynamics by representing all situations the same way, whether they represent emitters or not.

154 Additionally, systematic artifacts concerning advection processes were reported over regions with complex to-
155 pographies, particularly when high tropospheric vertical column densities are observed over mountainous regions.
156 These high values can hinder the identification and quantification of point sources, possibly due to inaccurate mean
157 wind fields over mountains. A study by Sun (2022) shows that these patterns can also be caused by 3D transport
158 effects which have been ignored in the simplified 2D approach which has been described so far. A "topography-wind"
159 V term can be introduced in Equation 3 in order to correct for this effect using ground wind $\mathbf{w}_g$, the topography
160 gradient ∇z_0, and an inverse scale height X_e as follows:

$$V = X_e \Omega' \mathbf{w}_g \cdot \nabla z_0 \qquad (4)$$

161 Here, we choose a uniform and constant value of $X_e = 0.3$ km^{-1}. This value corresponds to the mean inverse scale
162 used by Sun (2022) who allowed for a variability for X_e by fitting its value using observational data through linear
163 regressions. While we acknowledge the fact that choosing a single value for X_e is a simplification, we note that
164 performing the fit of its value would require an arbitrary selection of the cells used for that fit. We therefore compute
165 the following equation to estimate NO_x emissions:

$$E_{NO_x} = \mathcal{L}(\frac{\partial(\Omega u)}{\partial x} + \frac{\partial(\Omega v)}{\partial y} + k_{OH+NO_2}[OH] + X_e \Omega' \mathbf{w}_g \cdot \nabla z_0) \qquad (5)$$

166 Following de Foy and Schauer (2022), we perform the calculation of derivatives directly on the original TROPOMI grid
167 (along-track and across-track) to better handle pixels with low-quality or no data, resulting in lower discontinuities in
168 the calculated transport term. To do so, we re-grid the wind field on the TROPOMI grid and linearly interpolate the
169 estimates at the satellite timestamp. We do the same for all other parameters that are concerned for the calculation of
170 the sink term (concentrations of OH, NO and NO_2, and temperature). Emissions are thus calculated on the TROPOMI
171 grid and are then re-gridded on a regular north-south/east-west grid with a $0.0625° \times 0.0625°$ resolution.

172 Finally, the accuracy of TROPOMI retrievals can be compromised by challenges in estimating the air mass factor
173 or local effects, particularly in specific vertical distribution scenarios (Griffin et al., 2019; Lorente et al., 2019; Judd
174 et al., 2020). The latest versions of TROPOMI (v2.x) showed VCD values higher than those of earlier versions (v1.x),
175 with biases up to 40%, depending on pollution levels and seasonal variations (Van Geffen et al., 2022). Additionally, the
176 chemistry-transport model TM5, which is integrated into the operational TROPOMI product, tends to underestimate
177 pollution near the ground, while overestimating NO_2 concentrations at higher altitudes over the sea (Latsch et al.,
178 2023; Rieß et al., 2023). To compensate for such effects, studies like Goldberg et al. (2022) or Beirle et al. (2023)
179 corrected the used VCDs by changing the corresponding vertical sensitivity over emitters. In this study, we do not
180 perform such adjustment, while recognizing it could constitute a further step in the improvement of our dataset. On
181 Figure 1, we sum up the functioning of our method.
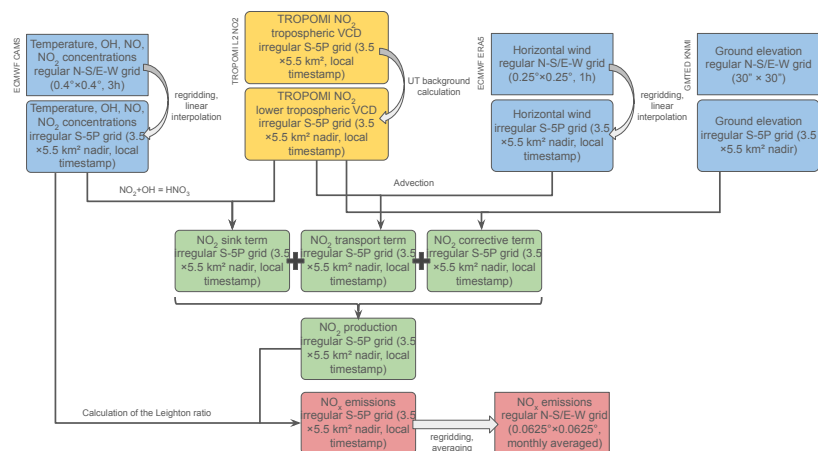
Figure 1: General overview of the mass-balance inversion.

2.3 EDGAR bottom-up inventory

Many high-resolution datasets for air quality exist at global (Benkovitz et al., 1996; Granier et al., 2019) or regional scale (Kuenen et al., 2022; He, 2012). Here we compare our averaged emissions for the year 2022 to NO_x emissions provided by The Emissions Database for Global Atmospheric Research (EDGARv6.1) for 2018. It is a global inventory providing $0.1° \times 0.1°$ gridded emissions of greenhouse gases and air pollutants at the monthly scale, covering different sectors (Crippa et al., 2020). It is based on activity data of different nature (population, industrial processes, energy production, fossil fuel extraction, agricultural outputs, etc.) derived from the International Energy Agency (IEA) and the Food and Agriculture Organization (FAO), and the emission factors corresponding to each of the covered sectors. National and regional information on technology mix data provide a better characterization of these emission factors. End-of-pipe measurements are also used for correcting purposes. The version 6.1 of the inventory covers the years 1970-2018.

3 Technical validation

3.1 Spatial distribution of the global NO_x emissions

The global map of the averaged NO_x emissions for 2022 is shown on Figure 2. Emissions are represented as density, i.e. by surface unit. The map is characterized by significant regional differences. The highest values are concentrated in developing areas such as south-eastern China, India and the Middle East. High values are also found in Europe, Russia and the United States, where they correspond to megacities and industrial areas. Transport emissions can also be highlighted where they provide the highest share of emissions, i.e. on highways and shipping lanes which appear in various regions. South America, Oceania and Sub-Saharan Africa display low or zero emissions except in a small number of cities and industrial sites. Wildfires, which are frequent in rainforests and savannas (Mebust and Cohen, 2013; Castellanos et al., 2014; Ossohou et al., 2019; Opacka et al., 2022), display quasi-zero emissions in Amazonia and low emissions in the Congo basin. Figure 3 zooms over seven macro-regions that cover most of the emitters over land and sea.

Generally speaking, the maps highlights the industrialized areas, revealing the world's main megacities where several sources of emissions (traffic, power, residential) are mixed. Some industrial facilities and large power plants also appear. Emissions are correctly resolved in most regions of the world. The observed spread of emissions over two to three pixels (i.e. about 12 to 20 km) further away from the exact location of the corresponding emitters is due to the turbulent spread of emissions, which is not considered in our method. Finally, we note that emissions in mid- and high-latitude regions (beyond about 40° from the Equator) seem to be noisy, due to an averaging over a smaller number of clear-sky days throughout the year. On average, countries such as Egypt, Niger and Saudi Arabia are observed more than 90% of the time with a quality flag higher than $q_{a,\lim} = 0.75$, while Ireland, Canada and Finland are observed less than 30% of the time. This uneven sampling is also present in tropical regions where rainfall

214 is frequent, as there is no measurement during cloudy scenes. Countries like Gabon, Indonesia or Peru are seen on
215 average less than 40% of the time with quality flags higher than the threshold. In some cases, this low density of
216 observations prevents emissions from intense sources from being quantified correctly at the monthly scale, as it is
217 discussed in Section 3.4.
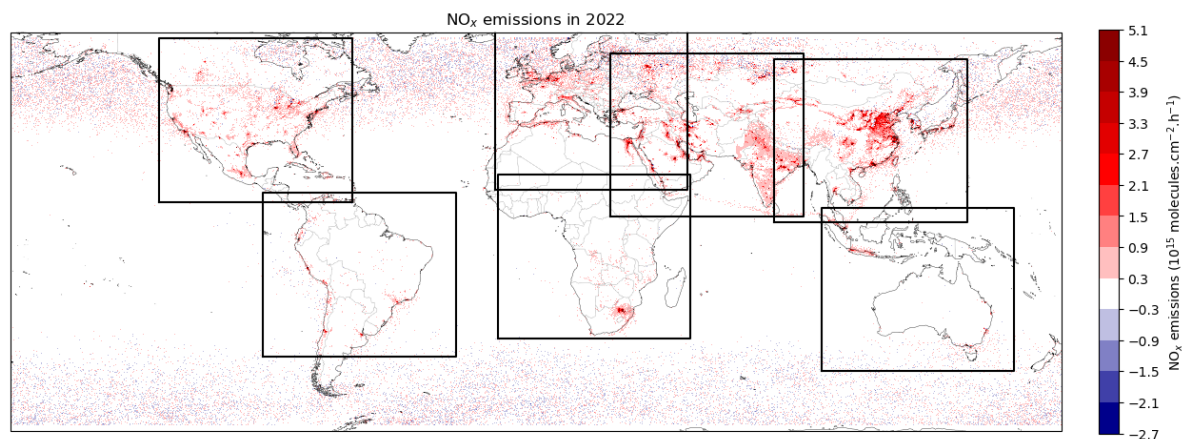
Figure 2: TROPOMI-derived mean daytime NO_x emission rates in 2022 estimated with the flux-divergence method. The seven frames correspond to macro-regions whose emissions are specifically shown in Figure 3.

218 The statistical distribution of emissions is shown in Figure 4. Four different regimes of emissions can be distinguished
219 in the red curve (note the log-log scale):

220 • Very low values of emission densities (less than ~0.02 Pmolecules.cm^{-2}.h^{-1}), in practice at places where there
221 are almost no emissions in reality. Note that, as the calculated fluxes represent averaged emissions, such pixels
222 can also represent places where high emissions occurred, but only during a small portion of the year, as it is the
223 case in regions where wildfires frequently happen.

224 • Residual emission densities (between ~0.02 Pmolecules.cm^{-2}.h^{-1} and ~0.2 Pmolecules.cm^{-2}.h^{-1}), for which it
225 is difficult to determine the corresponding source.

226 • Low emission densities (between ~0.2 and ~2 Pmolecules.cm^{-2}.h^{-1}), generally high enough to be associated
227 with an emitter, but too low for a reliable quantification to be possible unless heavy averaging. The upper limit
228 corresponds approximately to the emission densities observed on smaller power plants.

229 • High emission densities (higher than 2 Pmolecules.cm^{-2}.h^{-1}), where the signal-to-noise ratio is high enough to
230 quantify emissions when enough observations are averaged.

231 Figure 4 also shows negative values (blue curve), even though negative emissions are physically impossible.
232 They appear in practice because the transport term, which includes a derivative, can be negative. In calculated
233 emission densities, negative pixels of low absolute value are as numerous as positive pixels of the same amplitude;
234 they correspond to numerical noise and are found in pollution-free zones where the sink term is virtually zero. Higher
235 values for negative pixels are less frequent: we count about 4 times less pixels with emission densities lower than -0.2
236 Pmolecules.cm^{-2}.h^{-1} than pixels with emission densities higher than 0.2 Pmolecules.cm^{-2}.h^{-1} (yellow and red parts
237 of the graph in Figure 4). The locations where such high values are observed for negative pixels correspond to areas
238 close to anthropogenic sources of NO_x, but in situations for which the absolute transport term has been overestimated
239 or the sink term has been underestimated. Such negative emissions are limited to rare cases, such as Tehran, which
240 will be discussed in Section 4.2.
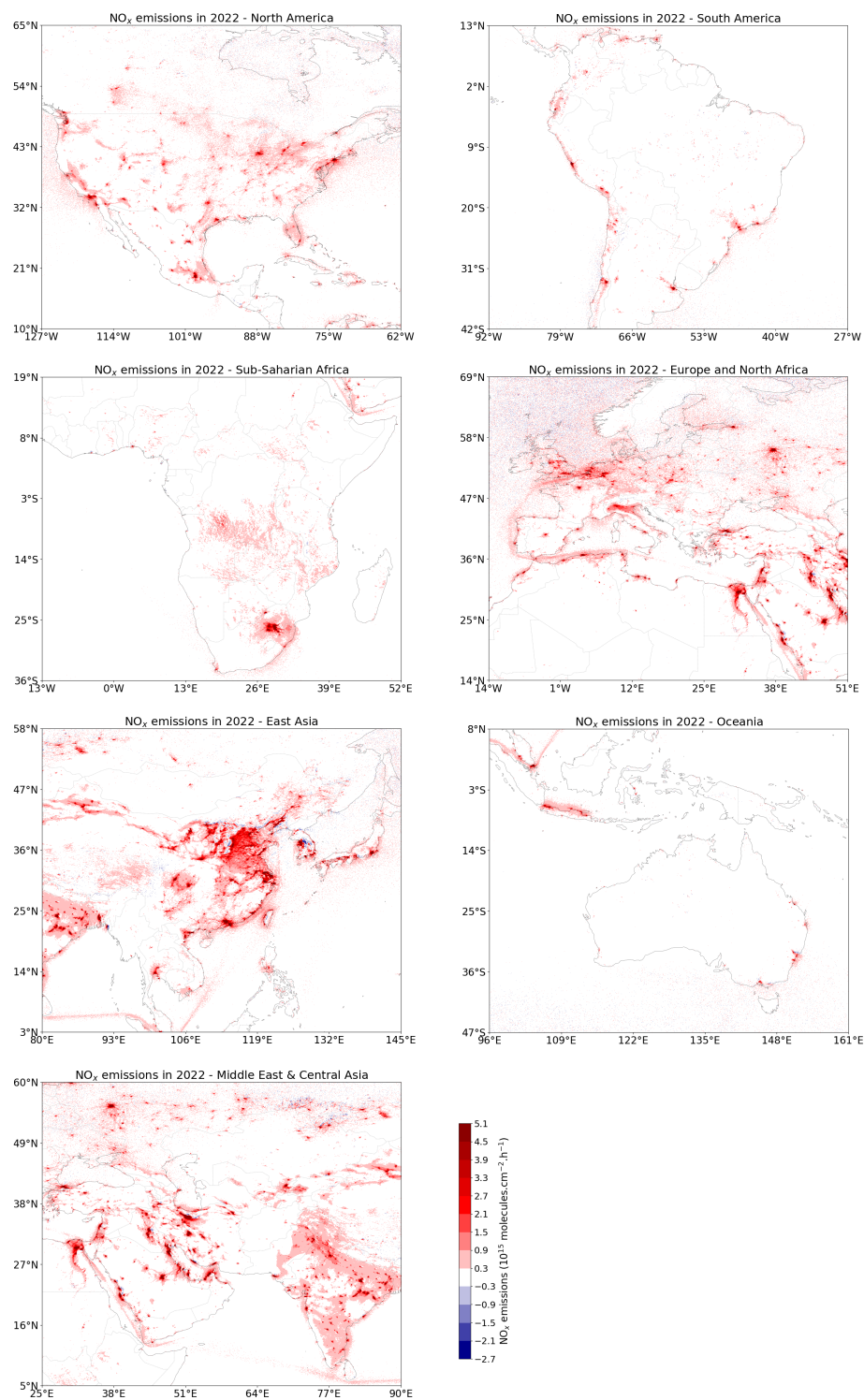
Figure 3: TROPOMI-derived mean daytime NO_x emission rates in 2022 estimated with the flux-divergence method for North America, South America, Sub-Saharan Africa, Europe and North Africa, East Asia, Oceania, Middle East and Central Asia.
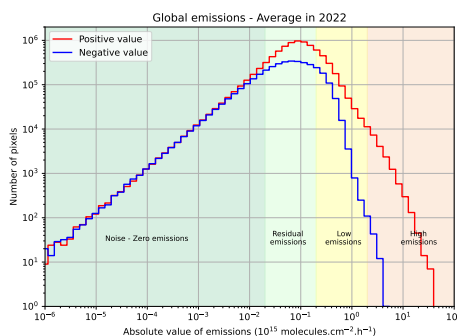
Figure 4: Distribution of positive and negative TROPOMI-inferred NO_x emissions for year 2022. Four regimes can be distinguished (the values defining the thresholds between these regimes are given as order of magnitudes).

3.2 Diffuse sources and point sources

The assimilation of high-resolution observations with the flux-divergence method holds a significant potential for pinpointing emissions at small scale. As a consequence, it reveals the difference between sources that emit pollutants from a localized area, called point sources, from diffuse sources emitting pollutants over a wider area, such as sprawling urban regions like megacities. While the extent of the observed NO_2 pollution created by a point source is primarily determined by advection and turbulent mixing, the spread of the pollution for a diffuse source is above all determined by the spatial extent of the source itself. Point sources are therefore characterized by a dominance of the transport term, while diffuse sources (the term "area sources" is also used) exhibit a balance or dominance of the sink term (Beirle et al., 2019). Within the flux-divergence method, these two types of sources can be identified differently, since the main sources of uncertainty come from wind angle in the case of a point source while they come from the OH concentration explaining the sink term for a diffuse source. Because this distinction remains qualitative, to classify a detected source as one or the other type, arbitrary thresholds must be defined, concerning the number of pixels above a certain value of emissions, or the share of the transport term within the emissions in Equation 5. Here, we catalog all sources in the averaged emissions map for 2022. Firstly, we define a source as a cluster of at least 3 contiguous pixels above the value of 2 $Pmolecules.cm^{-2}.h^{-1}$. We then classify these sources as "point" or "diffuse" according to the number of pixels in the detected cluster: point sources being the clusters comprising 3 to 9 pixels, and diffuse sources those with more than 10 pixels. We detected 456 point sources and 330 diffuse sources, whose locations are displayed on Figure 5. The detailed distribution is given in Supplementary Materials and in Rey-Pommier et al. (2024).
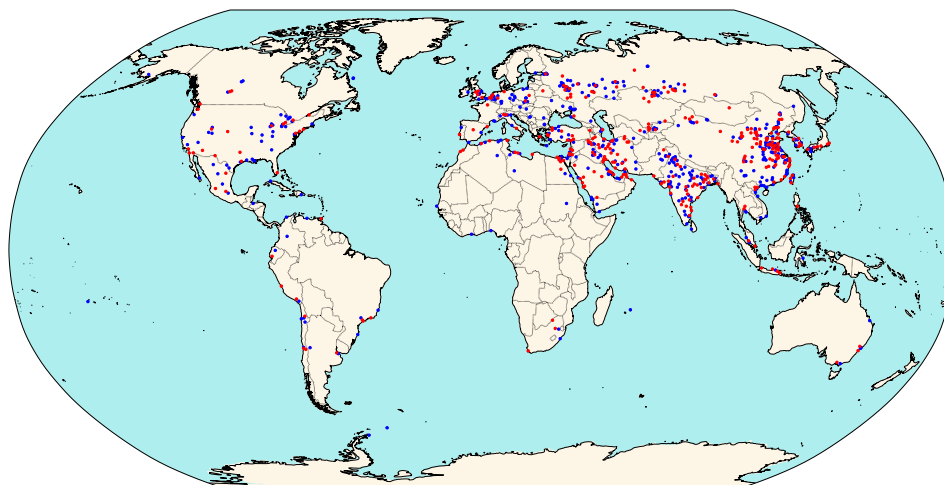
Figure 5: Location of different point sources in blue (between 3 and 9 contiguous pixels above 2 $Pmolecules.cm^{-2}.h^{-1}$) and diffuse sources in red (more than 10 contiguous pixels) for 2022.

3.2.1 Diffuse sources

Most point sources correspond to facilities such as power stations, cement kilns or mining sites. They can also correspond to concentrated urban areas. Conversely, almost all diffuse sources correspond to urban areas of megacities, whether they comprise industrial facilities within their extent or not. Exceptions concern mega-emitters like the Medupi and Matimba power plants in South Africa, mentioned in various articles (Reuter et al., 2019; Hakkarainen et al., 2021; Cusworth et al., 2023) or the Ain Sokhna industrial area in Egypt, already mentioned in Rey-Pommier et al. (2022). In both cases, such groups of industrial facilities exhibit particularly high emissions over more than 10 pixels and are detected as diffuse sources. Figure 6 displays the emissions of diffuse sources corresponding to megacities: Baghdad (32.9 t.h^{-1}, 198 pixels), Istanbul (16.3 t.h^{-1}, 132 pixels), Mexico City (17.4 t.h^{-1}, 111 pixels), Moscow (20.4 t.h^{-1}, 180 pixels), Riyadh (33.1 t.h^{-1}, 172 pixels) and Shanghai (102.0 t.h^{-1}, 837 pixels). Table 1 shows the 20 diffuse sources with the highest emissions.
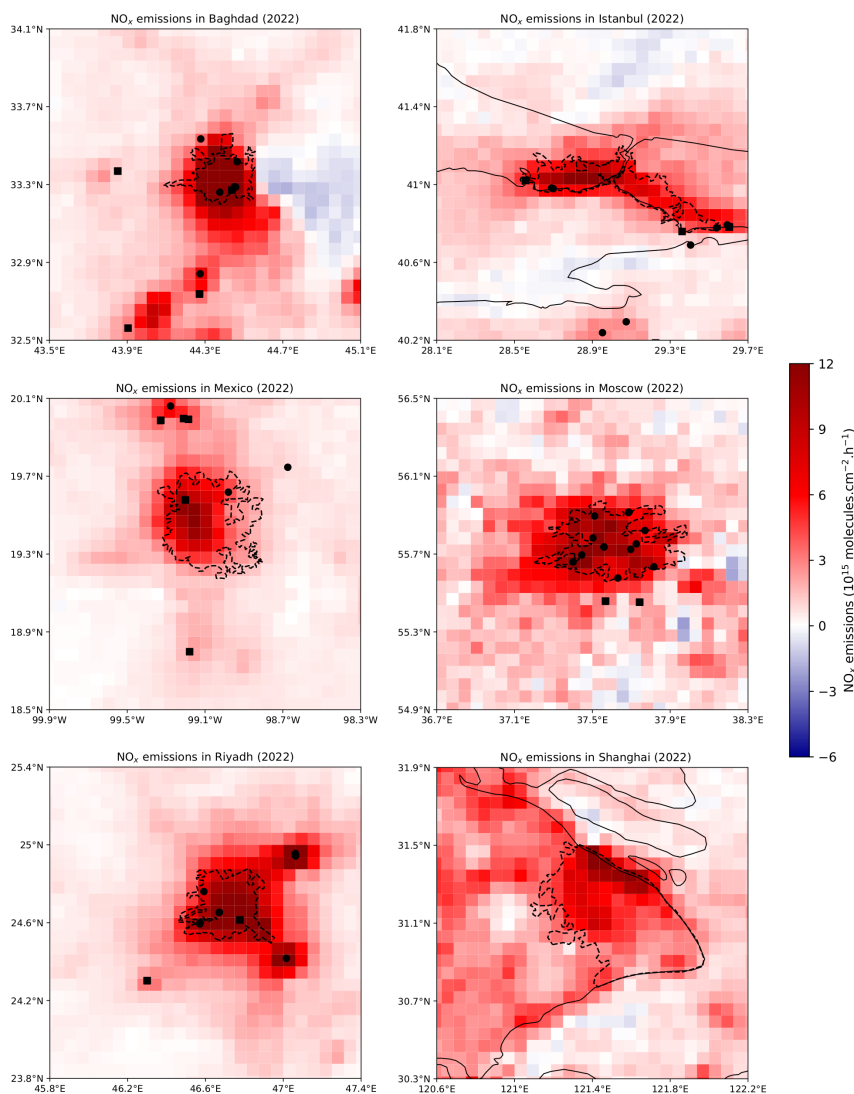
Figure 6: Map of mean daytime TROPOMI-inferred NO$_x$ emissions for 2022 for six megacities (diffuse sources), clockwise: Baghdad, Istanbul, Moscow, Shanghai, Riyadh, and Mexico City. The approximate boundaries of the cities are denoted with dashed lines and the location of power plants and cement plants are denoted with circles and squares respectively, except for Shanghai (unavailable data).

These six diffuse sources differ greatly from one another: Baghdad, Mexico City and Riyadh are very dense and isolated, allowing their emissions to stand out from the rest of the hotspots, while Moscow and Istanbul are less dense, resulting in lower emission densities. The Shanghai urban area has a large spatial extent, and the associated cluster extends over an area much wider than the city limits. Finally, it should be noted that Moscow and Shanghai experience many cloudy days, resulting in a fairly low level of averaging, leading to numerical noise that is visible on the maps. Our averaging also explains the absence of high annual emissions due to wildfires in our analysis. At a lower temporal scale however, wildfire emissions display an annual variability without significant outliers. The example of the rainforest in the Congo basin is studied in the Supplementary Materials, with emissions higher than the 2 Pmolecules.cm^{-2}.h^{-1} threshold during summer (JJA).

Number of pixels in cluster	Latitude (°N)	Longitude (°E)	Mean emission density (Pmolecules.cm^{-2}.h^{-1})	Output (t.h^{-1})	Emitter
2818	37.527	116.010	2.827	235.03	Beijing urban area, China
837	31.283	120.352	3.834	102.01	Shangai urban area, China
439	35.549	51.329	7.089	94.19	Tehran urban area, Iran
552	-26.406	28.739	4.266	78.45	Gauteng coal region, South Africa
425	22.798	113.630	3.721	54.22	Shenzen & Hong-Kong urban area, China
361	29.653	31.126	4.127	48.16	Cairo & Beni Suef urban area, Egypt
303	29.582	47.874	4.555	44.64	Kuwait City urban area, Kuwait
172	24.649	46.797	5.695	33.12	Riyadh urban area, Saudi Arabia
198	32.771	44.298	5.319	32.94	Baghdad urban area, Iraq
274	41.174	123.033	4.286	32.88	Anshan urban area, China
353	39.338	110.656	2.986	30.32	Ordos mining region, China
224	37.162	126.874	4.312	28.63	Seoul urban area, South Korea
171	25.316	55.342	4.809	27.65	Dubai urban area, United Arab Emirates
157	32.577	51.610	4.860	23.92	Ispahan urban and industrial area, Iran
127	21.115	39.309	4.916	21.66	Djeddah urban area, Saudi Arabia
219	37.317	112.087	3.173	20.56	Shanxi urban area, China
180	55.715	37.501	5.395	20.35	Moscow urban area, Russia
102	24.118	82.747	5.530	19.15	Jogi Chaura industrial zone, India
154	39.329	106.809	4.258	18.87	Wuhai/Hainan industrial zone, China
83	-12.183	-76.853	6.189	18.68	Lima urban area & Pachamac mines, Peru

Table 1: List and location of the 20 diffuse sources with highest TROPOMI-inferred NO$_x$ emissions, and corresponding size of the cluster and main sector responsible for the emissions.

3.2.2 Point sources

With a manual verification of the 456 detected point sources, we identify 61 outliers, 30 of which being points in places totally empty from any anthropogenic activity, and 31 points in areas with anthropogenic activity but without significant source (no facility of significant size). Most of these outliers are located in high-latitude regions, with 34 of them being located north to the 50°N parallel.

Because a threshold has been introduced in the classification of emitters, sources classified as "point sources" are isolated from other emitters, and their emissions constitute a peak in the displayed map. With a threshold set at 2 Pmolecules.cm^{-2}.h^{-1}, the corresponding signal-to-noise is generally high enough to perform a peak-fitting around the source. Since the observed spread of the emissions around the source is given by turbulent diffusion, we try to fit a 2D-Gaussian function on the detected point sources over a zone of 14 × 14 pixels around the detected maximum emission density within the corresponding cluster. Three examples are shown for the city of Medina, Saudi Arabia, the Shar Industrial zone, Oman and the Western Mountain power plant, Libya on Figure 7. Note that these locations correspond to point sources well-isolated from other industrial activities, in countries with frequent cloud-free conditions that allowed an averaging over a high number of days in 2022.

We acknowledge the fact that the value of 2 Pmolecules.cm^{-2}.h^{-1} to mark the limit between high and low emissions is arbitrary, as other values for this threshold could be used. For instance, the Beijing cluster, identified on Table 1, with a size of 2818 pixels respectively, is broke down into 31 smaller clusters (12 diffuse sources and 19 point sources) when changing the threshold from 2 Pmolecules.cm^{-2}.h^{-1} to 3 Pmolecules.cm^{-2}.h^{-1}. These new clusters represent better urban sprawling around the various megacities and industrial facilities in Eastern China. However, in the same regions, three point sources disappear when performing this threshold change. Such differences are displayed in the Supplementary Materials. To determine the sensitivity of the point source and diffuse source detection and classification method, we carry out the detection by changing this threshold from 2 Pmolecules.cm^{-2}.h^{-1} to 3 and 4 Pmolecules.cm^{-2}.h^{-1}. The point sources and diffuse sources are identified, and a fit with a 2D-Gaussian is carried

out on point sources to estimate better emissions by accounting for the Gaussian nature of turbulent diffusion around
the source. We then count the number of point sources with a fit of correct quality (with a correlation coefficient R^2
higher than 0.4). The results are shown in Table 2 for the different thresholds, and we compare the countries with the
most point sources. Note that among the 61 outliers identified in the detected point sources with the threshold of 2
Pmolecules.cm^{-2}.h^{-1}, only 10 reached a value of R^2 higher than 0.4.
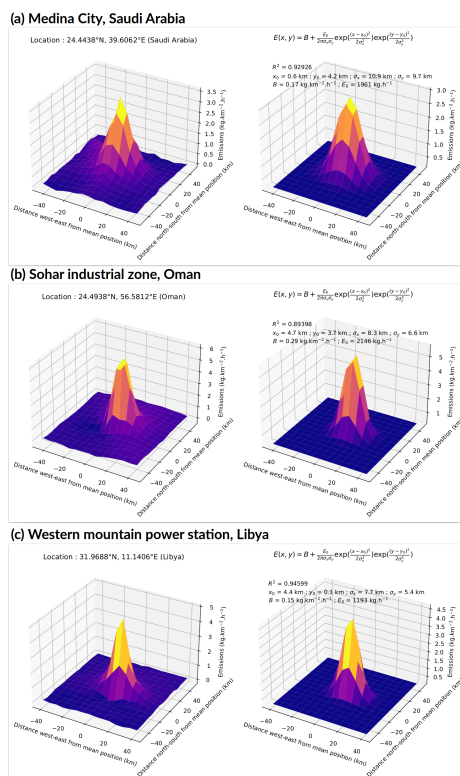
Figure 7: Calculated mean daytime NO$_x$ emissions in 2022 for point sources (left) and fitted emissions using a 2D-Gaussian function (right)
for the city of Medina, Saudi Arabia (a), the Sohar Industrial Zone, Oman (b) and the Western Mountain power plant, Libya (c).

Threshold value	2 Pmolecules.cm^{-2}.h^{-1}	3 Pmolecules.cm^{-2}.h^{-1}	4 Pmolecules.cm^{-2}.h^{-1}
Number of point sources	**456**	**303**	**172**
Point sources with $R^2 > 0.4$	**237**	**189**	**114**
China	24	27	18
India	37	33	22
Russia	23	18	12
United States	18	6	3
Türkiye	7	6	1
Iran	7	9	9
Saudi Arabia	5	5	5
Japan	2	5	4
Egypt	3	2	4
Germany	6	3	1
Iraq	5	5	2
Mexico	7	5	3
Algeria	5	2	0
Pakistan	5	1	2

Table 2: Analysis of the number of point sources detected as a function of the threshold applied for cluster detection, and the number of
point sources whose fit with a 2D-Gaussian was of acceptable quality ($R^2 > 0.4$). Countries with at least 5 point sources with one of the
thresholds are displayed.

As seen with the example of Beijing, moving to a higher threshold can reduce the number of point sources by not including some emitters with lower emissions, but it can also increase the number of detected point sources by reducing the number of pixels corresponding to the cluster and moving certain emitters from the "diffuse source" category to the "point source" category. For example, with a limit of 2 Pmolecules.cm^{-2}.h^{-1}, the group of the Ras Laffan power stations in Qatar does not appear as a point source because its emissions are associated to a greater cluster corresponding to a diffuse source which includes the nearby Doha megacity. Conversely, with limits of 3 or 4 Pmolecules.cm^{-2}.h^{-1}, these power plants appear as a point source, and a good quality Gaussian fit provides their total emissions of 1.69 t.h^{-1}, close to the value of 1.86.h^{-1} reported for the four-year average between 2019 and 2022 in Rey-Pommier et al. (2023). Finally, it should be noted that lowering the threshold to 1 Pmolecules.cm^{-2}.h^{-1} also reduces the number of diffuse sources because several nearby urban areas become linked by residual emission zones into a single, larger, diffuse source. Conversely, lowering the threshold detects a very large number of source points, but many of these additional points are outliers. In the rest of the study, we therefore choose to keep the lowest value of the threshold, i.e. 2 Pmolecules.cm^{-2}.h^{-1}, to optimise the number of correct emitters we work with. These emitters account for a total output of 2,388 t.h^{-1} (370 t.h^{-1} for point sources and 2018 t.h^{-1} for diffuse sources). This represents about 17% of all emissions with densities higher than 0.2 Pmolecules.cm^{-2}.h^{-1} (with a total output of 14,335 t.h^{-1}). As urban areas with more than 1 million inhabitants gather around 16% of the global population (Zimmer et al., 2023), this share of emissions from point and diffuse sources seems consistent with the detection limit of the flux-divergence method using TROPOMI retrievals, as urban areas lower than 1 million inhabitants are generally not detected as diffuse sources here.

The full list of the 456 point sources and 330 diffuse sources are given in Supplementary Materials. This list can be compared with the catalog provided by Beirle et al. (2023). Of the 237 point sources for which the Gaussian fit is of correct quality (with $R^2 > 0.4$), 144 also appear in their catalog. For these points, we generally obtain higher emissions (with a median of 409 t.h^{-1} and an average of 479 t.h^{-1} in our case, whereas they have a median of 296 t.h^{-1} and an average of 344 t.h^{-1}). The two datasets have no particular reason to exhibit any clear correlation because they concern different years, and because while their approach focused on monthly averages, ours presents annual averages. For example, a site designated as a point source by Beirle et al. (2023) might not be detected if averaged over a whole year, especially if it stays inactive during certain periods. For instance, their catalog shows 187 occurrences where the signal of NO$_x$ emissions was significant for 6 months out of 12, and 348 occurrences for 5 months.

3.3 National and regional outputs and comparison with bottom-up emissions

We perform an analysis of emissions at the scale of countries by comparing them to the NO$_x$ emissions provided by EDGARv6.1 for 2018. For our TROPOMI-inferred emissions, we calculate the total mean NO$_x$ output, representing daytime emissions for 2022, for each country using country masks at the 0.0625°×0.0625° resolution. To avoid any over-estimation of the total output due to a very high number of pixels with very low emissions, we exclude from the calculation pixels with emission densities below 0.2 Pmolecules.cm^{-2}.h^{-1}. For emissions in EDGARv6.1, we sum the gridded emissions, representing monthly averages in 2018, for all sectors covered by the inventory and calculate the average flux for the year 2018. The output for each country is calculated using country masks at the 0.1°×0.1° resolution. In both cases, we include pixels that directly touch coastlines because marine regions close to the shore see anthropogenic emissions spread due to turbulent diffusion. This can result in over-estimating total emissions for smaller countries, especially those with low emission densities. In order not to account for such outliers, we exclude countries with a population lower than 300,000 inhabitants or with a size lower than 1,000 km^2 from our analysis. This concerns many insular countries in the Caribbean and the Pacific, as well as micro-states like Andorra or Singapore. Figure 8 shows the country-wise comparison, covering 164 countries, and Table 3 provides a comparison at the scale of eight different macro-regions: Europe, North America and the Caribbean, South America, Middle East and North Africa, Former USSR countries, Oceania, Sub-Saharan Africa and the rest of Asia.

TROPOMI-inferred emissions are generally close to EDGAR estimates for high income level countries or countries with a majority of sources located in areas with high observation densities. This is the case for the three largest emitting countries, China, the United States and India, with TROPOMI-inferred emissions 11, 16 and 6% lower than EDGAR estimates respectively. These three countries account for 44% of global emissions. However, for the fourth highest emitting country, Russia, we estimate emissions 79% higher than EDGAR. We interpret this discrepancy as due to the low density of observations there, which leads to errors in calculating emissions over a large area. This is consistent with the large discrepancies found for many countries that also have low observation densities. The other countries for which the difference between our emissions and the EDGAR estimates is significant are low-income countries. It is possible that the sources there are small and difficult to detect with our method; it is also possible that the corresponding EDGAR estimates are imprecise, due to the incomplete or outdated nature of the reported sources in

361 these countries. The macro-regions with the highest discrepancies are thus Sub-Saharan Africa and the former USSR.
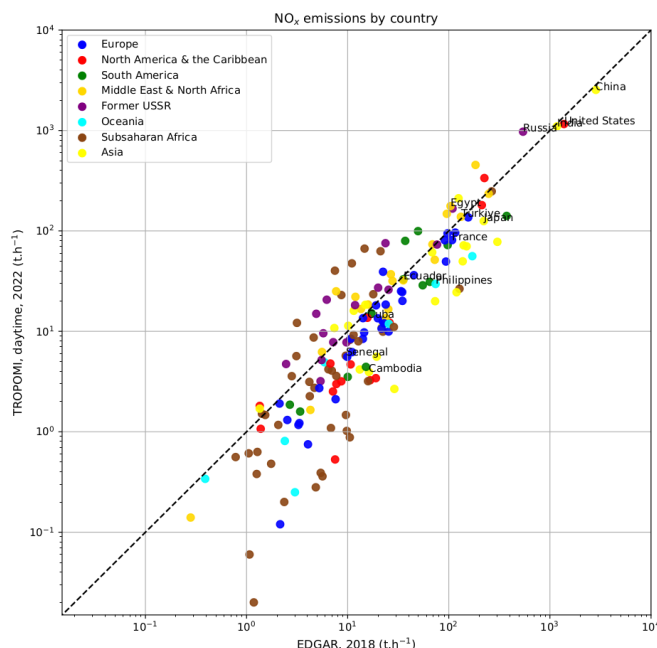
Figure 8: Comparison between TROPOMI-inferred daytime NO_x emissions for 2022 and mean emissions from EDGARv6.1 in 2018 for all countries, classified by macro-regions.

362 At the global scale, our TROPOMI-inferred daytime emissions for all considered countries (i.e., excluding emissions
363 which take place at sea and in smaller countries) reach a total value of 11,209 $t.h^{-1}$. This value is consistent with
364 that of EDGAR at 12,243 $t.h^{-1}$, i.e around 107 Mt per year, close to the value of 123 Mt calculated by Stocker (2014)
365 for global anthropogenic emissions in 2000 (which include shipping and aircraft emissions). We should however note
366 that our TROPOMI-inferred emissions only represent daytime emissions taken around 13:30 LT, which are generally
367 lower during mid-day than other times of the day, where pollution peaks in the early morning and late afternoon are
368 reported for most trafic in many cities and for power generation (Menut et al., 2012). Conversely, emissions during
369 daytime are generally much higher than nighttime emissions.

Region	TROPOMI 2022 ($t.h^{-1}$)	EDGAR 2018 ($t.h^{-1}$)	Relative bias VS EDGAR (weighted average)	Mean absolute error VS EDGAR (unweighted average)
Subsaharan Africa	656	702	-6.5 %	90.2%
Rest of Asia	4424	5482	-19.3 %	49.3%
Europe	842	1092	-22.9 %	38.7%
Middle East & North Africa	1509	1125	34.2 %	49.0%
North America & the Caribbean	1729	1944	-11.0 %	48.9%
Oceania	104	282	-63.2 %	52.6%
South America	512	762	-32.8 %	53.4%
Former USSR	1433	856	67.6 %	74.8%
Total	**11209**	**12243**	**-8.4 %**	**60.6%**

Table 3: Comparison between TROPOMI-inferred daytime NO_x emissions for 2022 and mean emissions from EDGARv6.1 in 2018 for macro-regions. For each macro-region, the relative bias between total TROPOMI-inferred emissions and total EDGAR emissions is calculated. The mean absolute bias for all countries of these macro-regions is also calculated.

370 ## 3.4 Temporal distribution and averaging size

371 The results presented so far concerned daytime emissions averaged on the entire year 2022 (at around 13:30 local
372 time for each pixel). They therefore show a certain potential for mapping the sources of pollution, quantifying the

corresponding emissions and characterising their type (by size and country or region). Several studies have shown the possibility to characterise a weekly cycle of NO_x emissions (Stavrakou et al., 2020; Rey-Pommier et al., 2022). The use of geostationary satellites, such as the Geostationnary Environment Monitoring Spectrometer (GEMS) in East Asia (Kim et al., 2020), the Tropospheric Emissions Monitoring of Pollution (TEMPO) in North America (Zoogman et al., 2017) and Sentinel-4 (launch planned in September 2024) in Europe (Gulde et al., 2017), could also prove promising for characterising the daily cycle of emissions, which would significantly improve forecasting capabilities. In our case, TROPOMI can only monitor pollution on a daily basis provided that retrievals are of high quality, and the analyses presented so far could theoretically be carried out at this temporal resolution. In practice however, the high sensitivity of the method to wind direction and the low signal-to-noise ratio around sources at high latitudes leads to daily emission maps that are very noisy in most cases, making it difficult to monitor activity at this temporal resolution. Averaging is therefore required to limit noise effects and limit the uncertainties associated to emission estimates. Here, we try to evaluate what level of averaging is necessary to limit noise effects and allow a monitoring of emissions. To this end, we consider the average daily emissions obtained for 2022 (i.e. over a maximum of 52 weeks) to be the most accurate estimate of daytime emissions. We compare this maximum averaging value with averages based on a smaller number of estimates. We compare the emissions of various emitters, calculated with an averaging period of 12, 24, 36 and 48 weeks. Figure 9 shows the results for diffuse sources, which are all urban areas, but with different latitudes, populations, levels of development and energy mixes: Ankara (Turkey), Cape Town (South Africa), Madrid (Spain), Portland (United States), Chaguanas (Trinidad and Tobago), Saint Petersburg (Russia), Manila (Philippines) and Muscat (Oman). Figure 10 shows the results for the source points, which are industrial facilities in Egypt, Australia, Mexico, Chile, India and Germany. The sources were chosen for their relative isolation from other sources. Calculated emissions correspond to the sum of pixels around the source with densities greater than 2 $Pmolecules.cm^{-2}.h^{-1}$. There are two pitfalls to be avoided in this comparison:

- The first pitfall would be not to account for the seasonal cycle of emissions, which is very pronounced in some cases, and to compare chronological averages. For example, comparing the first 12 weeks of the year with the first 24 weeks of the same year would not make sense in terms of the difference with emissions averaged over the whole year, because in the first case, emissions would essentially be calculated in boreal winter, whereas in the second case, emissions would be included during spring and summer. To avoid this seasonal bias, emissions averaged over 12 weeks correspond to an average over the first week of each of the 12 months of 2022, and emissions averaged over 24 weeks correspond to the first two weeks of these same 12 months, and so on.

- The second pitfall would be not to account for the weekly cycle of emissions. NO_x emissions are generally lower at weekends due to a reduction in human activity in most areas (i.e. on Saturday and Sunday, or Friday and Saturday in most Arabian and North-African countries). It is therefore necessary to ensure that the proportion of weekend days and weekdays in each of the averages calculated remains the same, hence the interest in averaging by weeks (these proportions are therefore 2/7 and 5/7 respectively). We also carry out a final set of averaging over 24 days, i.e. 2 days per month. Since the seasonal effect (first pitfall) is generally stronger than the weekly bias (second pitfall), we therefore choose to retain the principle of selecting the same number of days in each month, even if it means making comparisons between averages where the weekend and weekday rates differ by 2/7 and 5/7. This last averaging set will be indicated as "irregular".
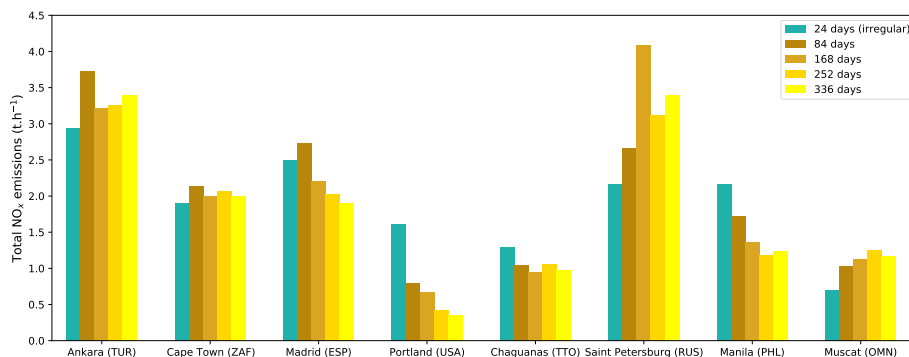
Figure 9: NO_x emissions for 8 different urban areas (diffuse sources), averaged over a period of 24, 84, 168, 252 and 336 days, evenly distributed throughout the year. The proportion of weekend days and weekdays is identical in all the averaging sets except the first one of 24 days.
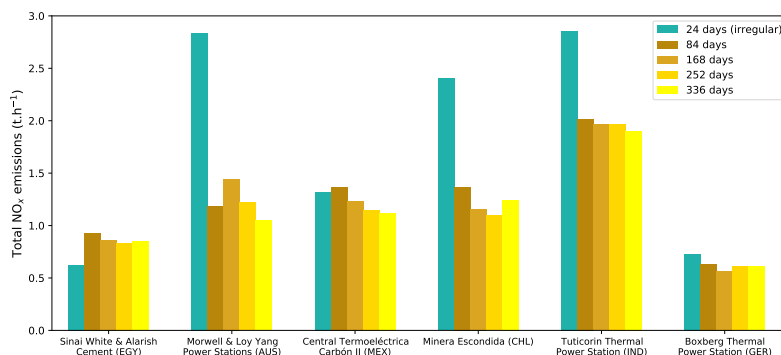
Figure 10: NO_x emissions for 8 different industrial facilities (diffuse sources), averaged over a period of 24, 84, 168, 252 and 336 days, evenly distributed throughout the year. The proportion of weekend days and weekdays is identical in all the averaging sets except for the first set of 24 days.

In the case of urban areas, the different averages uniformly distributed over time show a similarity in the emissions calculated over the time horizons for Ankara, Muscat, Cape Town, and, to a certain extent, Madrid. For these cities, the low cloud cover allows a high density of observations and optimal averaging. The 84-day averaging, and to some extent the 24-day irregular averaging, seems sufficient for monitoring emissions. This is not the case for the other urban areas studied, for which the observation density is lower, such as Manila, Saint Petersburg and, to a certain extent, Chaguanas. For these cities, emissions monitoring with averaging below 168 days (or even 252 days in the case of Saint Petersburg) is therefore limited by noise effects. In the case of the studied point sources, similar emissions are observed after an 84-day averaging. In some cases, a 24-day averaging is also sufficient, while in others it is not. The representativeness of emissions on such a low level of averaging should be considered with caution, as emissions from industrial plants are always more irregular than those from cities, with the exception of power stations used for baseload electricity generation. The averages over 84 days presented here represent emissions that include several days of activity and several moments of inactivity.

Overall, this analysis seems to indicate that tracking emissions from source points or diffuse sources using the flux-divergence method requires an averaging effort to limit the noise obtained in the daily emissions. This averaging effort, which increases with the density of observations, is of about a month in countries with frequent high-quality observations, but of about a quarter in regions with low observation densities, such as tropical regions and high-latitude regions.

4 Uncertainties and assessment of results

4.1 Model uncertainties

Our top-down emissions are calculated here using a flux-divergence model, based on a simplified calculation of a transport term, a sink term and a conversion factor from NO_2 to NO_x. This simplicity reduces the computation time to calculate emissions and the dependence on external datasets, at the cost of increased model uncertainties. Here, although a "topography-wind" term has been introduced in this article to refine the transport term, the sink term remains simple and only represents the reaction between NO_2 and OH. While this reaction is the first contributor of NO_x loss, other sinks may be significant. For instance, organic peroxy radicals can oxidise NO_x to form peroxy nitrates, making the corresponding sink important in the presence of VOCs (Stavrakou et al., 2013), especially in biomass fires. In different conditions, the formation of peroxyacetyl nitrate from NO_2 (Moxim et al., 1996), can also contribute to a significant share of the NO_x loss.

Another model uncertainty comes from the calculation of the conversion of NO_2 production to total NO_x. The majority of NO_x is emitted in the form of NO, which is not observed from space. A common assumption is that NO is rapidly transformed into NO_2 through its reaction with ozone, reaching a stationary state within a few minutes. Numerous studies (Beirle et al., 2019; de Foy and Schauer, 2022) assumed a photostationary state in typical urban conditions and used a ratio of 1.32 based on Seinfeld and Pandis (2006). Here, the values of this ratio calculated from CAMS data did not differ much from this value. However, the photostationary state is a hypothesis which is potentially not verified on the scale of a NO_x source like a power plant stack. Li et al. (2023b) calculated values of

this conversion ratio correlated with the combustion temperature and energy efficiency for sources in China that are highly intensive in energy such as power plants, and found a median value of 3.3. Biases in the calculation of the NO_x:NO_2 ratio can also arise in highly polluted environments, in which the Leighton relationship used to calculate this ratio is no longer valid. In particular, OH can also react with VOCs and form oxygenated VOCs. Further studies estimating this ratio at various spatial and temporal scales would thus provide a better implementation of our model.

4.2 Data uncertainties

The NO_2 column densities are the main input quantity in our estimation of NO_x emissions, making the its calculation within the TROPOMI product the first element to examine when considering the data uncertainties in our estimates. Columns are calculated from measurements of solar backscattered radiation and comparison with a specific UV-Visible band using the Differential Optical Absorption Spectroscopy method, before being assimilated to derive a tropospheric vertical component. The corresponding uncertainty under polluted conditions is dominated by the sensitivity of satellite observations to air masses near the ground, and is expressed through the calculation of the tropospheric air-mass factor (AMF). To assess the significance of such effects, vertical profiles within the TROPOMI product can be replaced by any other profile information, resulting in a new retrieved tropospheric NO_2 column. Douros et al. (2023) replaced the *a priori* TROPOMI OFFL NO_2 profile by high-resolution air quality forecasts for Europe. As compared to the standard TROPOMI NO_2 data, this new product was found to be biased-low by 5% to 12% for most European cities. The air mass factor (AMF) itself can be replaced: for instance, Lama et al. (2022) re-calculated the AMF by replacing the tropospheric AMF of the original TROPOMI OFFL product by an AMF taken from WRF-Chem simulations. Similarly, Beirle et al. (2023) re-calculated the AMF above different emitters from the corresponding averaging kernel based on a peak profile at plume height to better reflect the distribution of NO_2 close to ground, which resulted in an AMF correction of about 1.61. Here, we did not perform any of such corrections, and we consider a relative uncertainty for the column of 30% (Boersma et al., 2004), consistent with S-5P validation activities which indicate that TROPOMI tropospheric NO_2 columns are systematically biased low by about 30%–50% over cities (Verhoelst et al., 2021). Such a bias seems to run counter to our comparison with the catalog by (Beirle et al., 2023), for which this change in sensitivity was performed but leading to emissions generally lower than ours. A more detailed analysis of the concerned emitters seems necessary to better understand the parameters that have the largest impact on the vertical sensitivity of TROPOMI retrievals and our inversion model.

Other data uncertainties can arise from other parameters that play a crucial role in the estimation of advection and chemistry effects. An accurate representation of the wind is critical to estimate the transport term correctly. For a given plume, the poor representation of wind speed leads to an under-or over-estimation of transport, but the correct orientation of positive and negative values around the source remains. However, an incorrect representation of the wind direction, such as a non-alignment with the main direction of the plume, fails to represent a correct orientation of positive and negative values. The estimation of the transport term significantly thus relies heavily on the representation of the wind angle. Higher errors are therefore expected to be high in regions having winds that vary rapidly in time, or regions with complex horizontal wind variations, such as mountainous regions. In particular, situations where sub-grid scale-phenomena occur, not accounted for in ERA5 wind fields, might display even higher errors in the estimation of transported NO_x. For instance, Tehran, Iran, has an extremely complex topography, and in the calculated emissions, the transport term is particularly high compared with the sink term, with high and unrealistic negative values on large scales around the Tochal mountain immediately to the north of the city. Other megacities such as Seoul, South Korea, Jeddah, Saudi Arabia, Chittagong, Bangladesh, also exhibit unrealistically high values for the transport term. Such errors in the estimation of emission can also come from a wrong estimation of the air composition when calculating the sink term. The NO_2 lifetime relies heavily on the representation of the OH concentration field, which varies with NO_x itself through a non-linear mechanism. An incorrect representation of the sink term can occur at the scale of a plume by not capturing this relationship due to an incorrect knowledge of emitters on the ground. This can also be due to the 0.4°×0.4° resolution of CAMS that do not always capture the NO_2 gradients adequately in plumes near a known emitter (Valin et al., 2011; Li et al., 2023a). For the OH concentration, a relative uncertainty of 30% has been used (Huijnen et al., 2019), representing the largest component of absolute uncertainty apart from the vertical columns. Large errors in the annual cycle of OH, and therefore in the sink term, can thus be expected. As a consequence, a wrong estimation of wind angle and OH concentration can lead to unrealistically high emissions, or even negative emissions.

5 Conclusion

In this study, we present a global quantification of NO_x emissions by performing a mass-balance inversion based on the flux-divergence method, based. This approach offers a rapid alternative to traditional 3D inversion methods using Chemical Transport Models. The foundation of this method lies in the observation of tropospheric vertical column densities of NO_2 provided by TROPOMI. Our methodology incorporates several components in the calculation of emissions: a transport term driven by horizontal wind, a sink term largely driven by OH concentrations, and a topography-wind correction term. The emissions calculated represent mean daytime fluxes for the year 2022, allowing us to map emissions on a global scale. The results highlight that the primary sources of NO_x emissions are industrialized and developing countries. Our emission estimates are consistent with global estimates, as well as the EDGARv6.1 inventory, though notable discrepancies are observed at the national level, particularly in former USSR countries and sub-Saharan Africa. Besides, we performed a pinpointing of emitters by distinguishing between diffuse sources, typically large metropolitan areas with extensive spatial distribution (456 identified emitters), and point sources, generally isolated industrial facilities with emissions that often exhibit a Gaussian spread. 456 diffuse sources and 330 point sources are identified. Significant uncertainties remain, especially in regions where OH is not the only source of NO_x removal, regions where wind representation is inaccurate, and regions where TROPOMI data exhibit substantial biases. Nonetheless, our work demonstrates the feasibility of annual NO_x emission monitoring with reduced latency and fewer mis-allocation issues compared to traditional inventories. Our approach enables the monitoring of emissions at the monthly scale in regions with high observation densities, that usually correspond to dry, mid-latitude countries. Conversely, the effect of numerical noise, combined with low-observation densities, restricts such monitoring to a higher averaging period of up to months, generally in tropical and high-latitude regions. Efforts should be made to further develop this method to provide a near-real time monitoring tool a higher temporal resolution for these regions. The results of this study were obtained from the calculation of daily NO_x emissions in 2022 and their annual average.

6 Data availability

The monthly NO_x emission maps can be accessed at `https://doi.org/10.5281/zenodo.13957837` (Rey-Pommier et al., 2024). Data is made available as emission grid maps as `.nc` files with emissions expressed in petamolecules per square centimetre per hour ($Pmolecules.cm^{-2}.h^{-1}$). The lists of diffuse and point sources are also provided.

Author contributions. AR analysed the data, prepared the main software code and wrote the paper. AH improved some aspects of the code and prepared the code for Gaussian fitting. FC, PC, TC, JK and JS contributed to the improvement of the method and the interpretation of the results. All the authors read and agreed on the published version of the paper.

Financial support. This study has been funded by the European Union's Horizon 2020 research and innovation programme under grant agreement no. 856612 (EMME-CARE) and partially under grant agreement no. 958927 (Prototype System for a Copernicus CO2 Service (CoCO2)).

Competing interests. The authors declare no competing interests.

Ethical Approval. Not applicable.

Consent to Participate. Not applicable.

Consent to Publish. Not applicable.

References

Beirle, S., Borger, C., Dörner, S., Li, A., Hu, Z., Liu, F., Wang, Y., and Wagner, T. (2019). Pinpointing nitrogen oxide emissions from space, sci. adv., 5, eaax9800.

Beirle, S., Borger, C., Jost, A., and Wagner, T. (2023). Improved catalog of NOx point source emissions (version 2). *Earth System Science Data*, 15(7):3051–3073.

Benkovitz, C. M., Scholtz, M. T., Pacyna, J., Tarrasón, L., Dignon, J., Voldner, E. C., Spiro, P. A., Logan, J. A., and Graedel, T. (1996). Global gridded inventories of anthropogenic emissions of sulfur and nitrogen. *Journal of Geophysical Research: Atmospheres*, 101(D22):29239–29253.

Boersma, K., Eskes, H., and Brinksma, E. (2004). Error analysis for tropospheric NO2 retrieval from space. *Journal of Geophysical Research: Atmospheres*, 109(D4).

Burkholder, J., Sander, S., Abbatt, J., Barker, J., Cappa, C., Crounse, J., Dibble, T., Huie, R., Kolb, C., Kurylo, M., et al. (2020). Chemical kinetics and photochemical data for use in atmospheric studies; evaluation number 19. Technical report, Pasadena, CA: Jet Propulsion Laboratory, National Aeronautics and Space ....

Castellanos, P., Boersma, K., and Van Der Werf, G. (2014). Satellite observations indicate substantial spatiotemporal variability in biomass burning NOx emission factors for South America. *Atmospheric Chemistry and Physics*, 14(8):3929–3943.

Crippa, M., Guizzardi, D., Muntean, M., Schaaf, E., Solazzo, E., Monforti-Ferrario, F., Olivier, J., and Vignati, E. (2020). Fossil CO2 emissions of all world countries. *Luxembourg: European Commission*, pages 1–244.

Cusworth, D. H., Thorpe, A. K., Miller, C. E., Ayasse, A. K., Jiorle, R., Duren, R. M., Nassar, R., Mastrogiacomo, J.-P., and Nelson, R. R. (2023). Two years of satellite-based carbon dioxide emission quantification at the world's largest coal-fired power plants. *Atmospheric Chemistry and Physics*, 23(22):14577–14591.

Danielson, J. J. and Gesch, D. B. (2011). Global multi-resolution terrain elevation data 2010 (GMTED2010). Technical report, US Geological Survey.

de Foy, B. and Schauer, J. J. (2022). An improved understanding of NOx emissions in south asian megacities using tropomi NO2 retrievals. *Environmental Research Letters*, 17(2):024006.

Douros, J., Eskes, H., van Geffen, J., Boersma, K. F., Compernolle, S., Pinardi, G., Blechschmidt, A.-M., Peuch, V.-H., Colette, A., and Veefkind, P. (2023). Comparing Sentinel-5P TROPOMI NO2 column observations with the CAMS regional air quality ensemble. *Geoscientific Model Development*, 16(2):509–534.

Ehhalt, D. H., Rohrer, F., and Wahner, A. (1992). Sources and distribution of NOx in the upper troposphere at northern mid-latitudes. *Journal of Geophysical Research: Atmospheres*, 97(D4):3725–3738.

Eskes, H., van Geffen, J., Boersma, F., Eichmann, K., Apituley, A., Pedergnana, M., Sneep, M., Veefkind, J., and Loyola, D. (2022). *Sentinel-5 Precursor/TROPOMI Level 2 Product User Manual Nitrogen Dioxide*.

Goldberg, D. L., Harkey, M., de Foy, B., Judd, L., Johnson, J., Yarwood, G., and Holloway, T. (2022). Evaluating NOx emissions and their effect on O3 production in Texas using TROPOMI NO2 and HCHO. *Atmospheric Chemistry and Physics*, 22(16):10875–10900.

Graedel, T., Farrow, L., and Weber, T. (1976). Kinetic studies of the photochemistry of the urban troposphere. *Atmospheric Environment (1967)*, 10(12):1095–1116.

Granier, C., Darras, S., van der Gon, H. D., Jana, D., Elguindi, N., Bo, G., Michael, G., Marc, G., Jalkanen, J.-P., Kuenen, J., et al. (2019). *The Copernicus atmosphere monitoring service global and regional emissions (April 2019 version)*. PhD thesis, Copernicus Atmosphere Monitoring Service.

Griffin, D., Zhao, X., McLinden, C. A., Boersma, F., Bourassa, A., Dammers, E., Degenstein, D., Eskes, H., Fehr, L., Fioletov, V., et al. (2019). High-resolution mapping of nitrogen dioxide with TROPOMI: First results and validation over the canadian oil sands. *Geophysical Research Letters*, 46(2):1049–1060.

Gulde, S., Kolm, M., Smith, D., Maurer, R., Courrèges-Lacoste, G. B., Sallusti, M., and Bagnasco, G. (2017). Sentinel 4: A geostationary imaging UVN spectrometer for air quality monitoring: Status of design, performance and development. In *International Conference on Space Optics—ICSO 2014*, volume 10563, pages 1158–1166. SPIE.

Hakkarainen, J., Szeląg, M. E., Ialongo, I., Retscher, C., Oda, T., and Crisp, D. (2021). Analyzing nitrogen oxides to carbon dioxide emission ratios from space: A case study of Matimba Power Station in South Africa. *Atmospheric Environment: X*, 10:100110.

He, K. (2012). Multi-resolution Emission Inventory for China (MEIC): model framework and 1990-2010 anthropogenic emissions. In *AGU fall meeting abstracts*, volume 2012, pages A32B–05.

Hersbach, H., Bell, B., Berrisford, P., Hirahara, S., Horányi, A., Muñoz-Sabater, J., Nicolas, J., Peubey, C., Radu, R., Schepers, D., et al. (2020). The ERA5 global reanalysis. *Quarterly Journal of the Royal Meteorological Society*, 146(730):1999–2049.

Hoelzemann, J. J., Schultz, M. G., Brasseur, G. P., Granier, C., and Simon, M. (2004). Global wildland fire emission model (GWEM): Evaluating the use of global area burnt satellite data. *Journal of Geophysical Research: Atmospheres*, 109(D14).

Huijnen, V., Eskes, H., Wagner, A., Schulz, M., Christophe, Y., Ramonet, M., Basart, S., Benedictow, A., Blechschmidt, A.-M., Chabrillat, S., et al. (2016). Validation report of the CAMS near-real-time global atmospheric composition service: System evolution and performance statistics. Status up to 1 June 2016; `https://pure.mpg.de/rest/items/item_2441827/component/file_2441834/content`.

Huijnen, V., Pozzer, A., Arteta, J., Brasseur, G., Bouarar, I., Chabrillat, S., Christophe, Y., Doumbia, T., Flemming, J., Guth, J., et al. (2019). Quantifying uncertainties due to chemistry modelling–evaluation of tropospheric composition simulations in the CAMS model (cycle 43r1). *Geoscientific Model Development*, 12(4):1725–1752.

Judd, L. M., Al-Saadi, J. A., Szykman, J. J., Valin, L. C., Janz, S. J., Kowalewski, M. G., Eskes, H. J., Veefkind, J. P., Cede, A., Mueller, M., et al. (2020). Evaluating Sentinel-5P TROPOMI tropospheric NO2 column densities with airborne and Pandora spectrometers near New York City and Long Island Soun. *Atmospheric measurement techniques*, 13(11):6113–6140.

Kim, J., Jeong, U., Ahn, M.-H., Kim, J. H., Park, R. J., Lee, H., Song, C. H., Choi, Y.-S., Lee, K.-H., Yoo, J.-M., et al. (2020). New era of air quality monitoring from space: Geostationary Environment Monitoring Spectrometer (GEMS). *Bulletin of the American Meteorological Society*, 101(1):E1–E22.

Kuenen, J., Dellaert, S., Visschedijk, A., Jalkanen, J.-P., Super, I., and Denier van der Gon, H. (2022). CAMS-REG-v4: a state-of-the-art high-resolution european emission inventory for air quality modelling. *Earth System Science Data*, 14(2):491–515.

Lama, S., Houweling, S., Boersma, K. F., Aben, I., Denier van der Gon, H. A., and Krol, M. C. (2022). Estimation of OH in urban plumes using TROPOMI-inferred NO2/CO. *Atmospheric Chemistry and Physics*, 22(24):16053–16071.

Lama, S., Houweling, S., Boersma, K. F., Eskes, H., Aben, I., Denier van der Gon, H. A., Krol, M. C., Dolman, H., Borsdorff, T., and Lorente, A. (2020). Quantifying burning efficiency in megacities using the NO2/CO ratio from the Tropospheric Monitoring Instrument (TROPOMI). *Atmospheric Chemistry and Physics*, 20(17):10295–10310.

Latsch, M., Richter, A., and Burrows, J. P. (2023). Improving the detection of global NOx emissions from shipping in S5P/TROPOMI data. Technical report, Copernicus Meetings.

Li, C., Martin, R. V., Cohen, R. C., Bindle, L., Zhang, D., Chatterjee, D., Weng, H., and Lin, J. (2023a). Variable effects of spatial resolution on modeling of nitrogen oxides. *Atmospheric Chemistry and Physics*, 23(5):3031–3049.

Li, X., Cohen, J. B., Qin, K., Geng, H., Wu, X., Wu, L., Yang, C., Zhang, R., and Zhang, L. (2023b). Remotely sensed and surface measurement-derived mass-conserving inversion of daily NOx emissions and inferred combustion technologies in energy-rich northern china. *Atmospheric Chemistry and Physics*, 23(14):8001–8019.

Lorente, A., Boersma, K., Eskes, H., Veefkind, J., Van Geffen, J., De Zeeuw, M., Denier Van Der Gon, H., Beirle, S., and Krol, M. (2019). Quantification of nitrogen oxides emissions from build-up of pollution over Paris with TROPOMI. *Scientific reports*, 9(1):1–10.

Mebust, A. K. and Cohen, R. C. (2013). Observations of a seasonal cycle in NOx emissions from fires in african woody savannas. *Geophysical research letters*, 40(7):1451–1455.

Menut, L., Goussebaile, A., Bessagnet, B., Khvorostiyanov, D., and Ung, A. (2012). Impact of realistic hourly emissions profiles on air pollutants concentrations modelled with chimere. *Atmospheric environment*, 49:233–244.

Moxim, W., Levy, H., and Kasibhatla, P. (1996). Simulated global tropospheric PAN: Its transport and impact on NOx. *Journal of Geophysical Research: Atmospheres*, 101(D7):12621–12638.

628 Opacka, B., Müller, J.-F., and Stavrakou, T. (2022). Evaluation of soil NO emissions in the tropics using field data
629 and TROPOMI NO2 columns. In *EGU General Assembly Conference Abstracts*, pages EGU22–1287.

630 Ossohou, M., Galy-Lacaux, C., Yoboué, V., Hickman, J., Gardrat, E., Adon, M., Darras, S., Laouali, D., Akpo, A.,
631 Ouafo, M., et al. (2019). Trends and seasonal variability of atmospheric NO2 and HNO3 concentrations across
632 three major african biomes inferred from long-term series of ground-based and satellite measurements. *Atmospheric*
633 *Environment*, 207:148–166.

634 Platt, U., Stutz, J., Platt, U., and Stutz, J. (2008). *Differential absorption spectroscopy*. Springer.

635 Reuter, M., Buchwitz, M., Schneising, O., Krautwurst, S., O'Dell, C. W., Richter, A., Bovensmann, H., and Bur-
636 rows, J. P. (2019). Towards monitoring localized CO2 emissions from space: co-located regional CO2 and NO2
637 enhancements observed by the OCO-2 and S5P satellites. *Atmospheric Chemistry and Physics*, 19(14):9371–9383.

638 Rey-Pommier, A., Chevallier, F., Ciais, P., Broquet, G., Christoudias, T., Kushta, J., Hauglustaine, D., and Sciare, J.
639 (2022). Quantifying NOx emissions in Egypt using TROPOMI observations. *Atmospheric Chemistry and Physics*,
640 22(17):11505–11527.

641 Rey-Pommier, A., Chevallier, F., Ciais, P., Kushta, J., Christoudias, T., Bayram, I. S., and Sciare, J. (2023). De-
642 tecting nitrogen oxide emissions in Qatar and quantifying emission factors of gas-fired power plants–a 4-year study.
643 *Atmospheric Chemistry and Physics*, 23(21):13565–13583.

644 Rey-Pommier, A., Héraud, A., Chevallier, F., Ciais, P., Christoudias, T., Kushta, J., and Sciare, J. (2024). Global
645 gridded NOx emissions using TROPOMI observations. [Data set].

646 Rieß, T. C. V., van Vliet, J., Van Roy, W., de Laat, J., Dammers, E., and Boersma, F. (2023). Aircraft validation
647 reveals a 20% low bias in TROPOMI NO2 over sea caused by TM5 a priori profiles. Technical report, Copernicus
648 Meetings.

649 Seinfeld, J. H. and Pandis, S. N. (2006). Atmospheric chemistry and physics from air pollution to climate change.

650 Stavrakou, T., Müller, J.-F., Bauwens, M., Boersma, K., and van Geffen, J. (2020). Satellite evidence for changes in
651 the NO2 weekly cycle over large cities. *Scientific reports*, 10(1):1–9.

652 Stavrakou, T., Müller, J.-F., Boersma, K., Van Der A, R., Kurokawa, J., Ohara, T., and Zhang, Q. (2013). Key chem-
653 ical NOx sink uncertainties and how they influence top-down emissions of nitrogen oxides. *Atmospheric Chemistry*
654 *and Physics*, 13(17):9057–9082.

655 Stocker, T. (2014). *Climate change 2013: the physical science basis: Working Group I contribution to the Fifth*
656 *assessment report of the Intergovernmental Panel on Climate Change*. Cambridge University Press.

657 Sun, K. (2022). Derivation of emissions from satellite-observed column amounts and its application to TROPOMI
658 NO2 and CO observations. *Geophysical Research Letters*, 49(23):e2022GL101102.

659 Thornton, J. A., Virts, K. S., Holzworth, R. H., and Mitchell, T. P. (2017). Lightning enhancement over major oceanic
660 shipping lanes. *Geophysical Research Letters*, 44(17):9102–9111.

661 Valin, L., Russell, A., Hudman, R., and Cohen, R. (2011). Effects of model resolution on the interpretation of satellite
662 NO2 observations. *Atmospheric Chemistry and Physics*, 11(22):11647–11655.

663 Van Geffen, J., Eskes, H., Compernolle, S., Pinardi, G., Verhoelst, T., Lambert, J.-C., Sneep, M., Ter Linden, M.,
664 Ludewig, A., Boersma, K. F., et al. (2022). Sentinel-5P TROPOMI NO2 retrieval: impact of version v2.2 improve-
665 ments and comparisons with OMI and ground-based data. *Atmospheric Measurement Techniques*, 15(7):2037–2060.

666 Vandaele, A. C., Hermans, C., Simon, P. C., Carleer, M., Colin, R., Fally, S., Merienne, M.-F., Jenouvrier, A., and
667 Coquart, B. (1998). Measurements of the NO2 absorption cross-section from 42 000 cm-1 to 10 000 cm-1 (238–1000
668 nm) at 220 K and 294 K. *Journal of Quantitative Spectroscopy and Radiative Transfer*, 59(3-5):171–184.

669 Verhoelst, T., Compernolle, S., Pinardi, G., Lambert, J.-C., Eskes, H. J., Eichmann, K.-U., Fjæraa, A. M., Granville,
670 J., Niemeijer, S., Cede, A., et al. (2021). Ground-based validation of the Copernicus Sentinel-5p TROPOMI NO2
671 measurements with the NDACC ZSL-DOAS, MAX-DOAS and Pandonia global networks. *Atmospheric Measurement*
672 *Techniques*, 14(1):481–510.

673 Yienger, J. and Levy, H. (1995). Empirical model of global soil-biogenic NOx emissions. *Journal of Geophysical*
674 *Research: Atmospheres*, 100(D6):11447–11464.

675 Zimmer, A., C. T. N. B. A. G., J. Giezendanner. Palisades, N. N. S. D., and (SEDAC)., A. C. (2023). Global Urban
676 Demography Dataset (GUDD) (Preliminary Release). *https://doi.org/10.7927/4rjm-vf23*.

677 Zoogman, P., Liu, X., Suleiman, R., Pennington, W., Flittner, D., Al-Saadi, J., Hilton, B., Nicks, D., Newchurch,
678 M., Carr, J., et al. (2017). Tropospheric emissions: Monitoring of pollution (tempo). *Journal of Quantitative*
679 *Spectroscopy and Radiative Transfer*, 186:17–39.

680